Identification of subsonic *P*-waves

Paul Michaels*

ABSTRACT

A field trial was conducted to test the existence of sub-sonic ($V_p < 331$ m/s) *P*-waves previously reported in the literature. A 1-m-long reverse profile was acquired with three-component (3C) geophones on a sandy silt (unified classification ML). The silt had a porosity of 54%, a degree of water saturation of 63%, and a plasticity index of 10. No subsonic *P*-waves were observed, although high-frequency (up to 1200 Hz) Rayleigh waves were identified by hodogram analysis. These surface waves were observed with horizontal velocities that varied from 40 to 200 m/s. Hodogram observations and theory suggest that a portion of the data were also in the near-field.

INTRODUCTION

Reports of the detection of subsonic (<331 m/s) *P*-waves in shallow high-resolution seismic testing (Bachrach et al., 1998; Bachrach and Nur, 1998; and Baker et al., 1999) appear to be in conflict with recently published laboratory measurements on both dry and saturated soils at conditions of low effective stress (Khair and Ibrahim, 1999). Further, earlier crosshole and downhole studies by White and Sengbush (1953) conducted in loose sand reported significantly faster velocities than the more recent seismic testing. Motivated by these apparent discrepancies, I tested the hypothesis that *P*-waves commonly travel at subsonic velocities in near-surface soils, using an experiment scaled to a previously published case history (Baker et al., 1999). A major concern was that, in the absence of geophone arrays, a surface wave might be mistaken for a subsonic *P*-wave. To avoid such an error, I used three-component (3C) recording. By observing the particle motion, I hoped to have a better opportunity to classify the recorded waves properly.

Definition of terms and wave types

It would lead to a circular argument if wave velocity were used to identify the waves in this sort of study. Since the iden-tification of wave type is presented in terms of hodogram observations, the following comments are required.

A *P*-wave is one in which the major particle motion is in the direction of the wave propagation. Thus, for geophones on the surface, the direct wave should be most apparent on the horizontal, in-line component. A subsonic *P*-wave is meant to travel slower than the speed of a pressure wave in air (nominally 331 m/s). Subsonic is not meant to refer to the limits of the human ear.

An *S*-wave is one in which the major particle motion is orthogonal to the direction of wave propagation. Given a vertical impact point source, we expect primarily vertically polarized, or *SV*-waves, to propagate on the surface. These should be most apparent on the vertical component of a surface geophone.

Rayleigh waves are a mixture of both *P*- and *SV*-wave motion. As they travel at the surface boundary, the component *P*- and *SV*-waves exhibit elliptical motion (Aki and Richards, 1980, p. 161). The *P*- and *SV*-waves combine to produce a fundamental mode Rayleigh wave at the surface of a half-space which exhibits retrograde elliptical motion. Below the surface of the half-space at a depth of about 20% of the Rayleigh wave-length (White, 1983, p. 32), the Rayleigh-wave motion converts to prograde elliptical. The situation becomes more complex with velocity layering.

Finally, there are horizontally polarized, or *SH*-waves, and Love waves. The motion for these waves is most evident on the horizontal component, transverse to the direction of wave propagation.

One can influence the dominant type of radiation recorded with surface geophones by the choice of seismic source. The application of a transverse horizontal force to the soil favors *SH*- and Love waves. A vertical force, on the other hand, favors Rayleigh waves and is known as Lamb's problem (Lamb, 1904). The energy distribution radiated from a vertically oscillating disk on a half-space medium (Poisson's ratio, 0.25) is 67% Rayleigh waves, 26% *SV*-waves, and only 7% *P*-waves (Miller and Pursey, 1955). Since no geophone arrays were used in the work presented here, Rayleigh waves should dominate the vertical-component seismogram. One cannot assume that the first visible arrival will be a *P*-wave, since the *P*-wave

(if present) may be below the recording threshold of a system set conservatively to avoid clipping the Rayleigh wave. The appendix provides a discussion of Lamb's problem and illustrates the dominance of Rayleigh waves over horizontally propagating P- and SV-waves with synthetic seismograms.

The terms P- and S-waves are generally appropriate to the far-field. Near-field wave propagation includes motion that is a mixture of both P- and S-wave contributions. The gradual separation of P- and S-wave motion appears as a form of dispersion (Sanchez-Salinero et al., 1986). The extent of the near-field region from the source depends largely on the contrast between P- and S-wave velocities, the spectral bandwidth of the propagating wavelet, and the size of the source region compared to the wavelengths involved (Appendix).

Discussion of previous work

Khair and Ibrahim (1999) conducted laboratory measurements of P-waves under both dry and saturated conditions using a pulse technique. Figure 1 includes a replotting of a portion of their data (diamond symbols) for both a saturated and a dry medium sand. The grain diameters ranged from 0.25 to 0.5 mm, and porosity averaged 43%. The degree of saturation was <100%, producing slower-than-expected values for the saturated trials. The saturated trials did not repeat as well as the dry trials, presumably because of variations in the trapped air. On the other hand, the dry results were quite repeatable. Calibration on a water sample produced 1500 m/s.

The pressures used by Khair and Ibrahim (1999) correspond to stress conditions in the depth range extending from about 6 to 24 m. To fill in the gap from 0 to 6 m, field results from cross-hole testing have been added to Figure 1. These data were acquired from the surface to a depth of 24 m (White and Sengbush, 1953). The findings for loose sand have been plotted with circles. A mass density of 1700 kg/m³ was used to convert
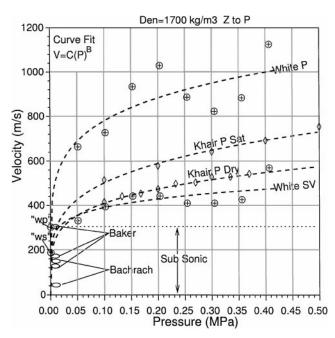

FIG. 1. Plot of laboratory velocities (after Khair and Ibrahim, 1999), downhole and crosshole velocities (White and Sengbush, 1953), and field-determined velocities (Baker et al., 1999; Bachrach et al., 1998). Dashed curves are for power law curve fitting (see Table 1).

depth to stress. No subsonic P-waves were recorded, even at the surface. White and Sengbush's surface P- and SV-wave velocity determinations are annotated wp and ws along the vertical axis of the plot.

White and Sengbush (1953) reported good agreement between the downhole P-wave velocities and those of the crosshole experiments, leading one to conclude that the material was fairly isotropic. Although it was not stated, we may assume that these were moist sands (not dry). In the same paper, a different data set was also presented for loose sand which included the transition across the water table. A significant jump in P-wave velocity was reported (1800 m/s P-waves below the water table, 1000 m/s just above the water table). Because of capillary forces, moist sands will support faster S-wave velocities than dry sands. The effect is most developed for water saturations in the range of 5% to 20% of void volume (Wu et al., 1984). The S-wave velocities presented by White and Sengbush (1953) may well represent this range of partial water saturation, since truly dry soil is rare (descending recharge or capillary fringe being a common source of soil moisture).

White and Sengbush (1953) interpret their velocities in terms of the uniformly packed spherical models that originated with the works of Hertz (1881), Mindlin (1949, 1954), Mindlin and Deresiewicz (1953), and Gassmann (1951a, b, 1953). In addition to Gassmann's hexagonal pack analysis, White (White and Sengbush 1953) added his own cubic pack presentation, discussing both P- and S-waves under dry conditions and P-waves under saturated conditions. Interest in uniformly packed sphere modeling continues to today (Cascante and Santamarina, 1996; Bachrach et al., 1998; Bachrach et al., 2000).

The assumptions invoked in the Hertz–Mindlin-Deresiewicz–Gassmann theories are generally these:

1) the grains are in the shape of uniform (all of the same radius) spheres;
2) the grains are not cemented but present a medium for wave propagation by virtue of contact friction between the grains; and
3) the pore spaces have a vacuum or are completely fluid filled (with either air or water). Except for Gassmann's open-system case, the fluid and frame are coupled (no relative motion). Partially water-saturated conditions were not addressed in these theories.

Given these assumptions, the velocity behavior is expected to be independent of sphere radius. The velocity equation for either P- or S-waves that results from these theories can be expressed in the following general form:

$$V = C(P)^B \qquad (1)$$

where V is velocity, P is pressure supported by the frame (effective stress), and C is a constant that depends on the packing details, porosity, and elastic properties of the grains and fluid. The theoretical value predicted for B is 1/6, and one can also replace pressure with depth below the surface. The conversion to depth involves using an effective unit weight for any given pack of spheres.

The dashed curves in Figure 1 are the result of least-squares curve fitting of the different data sets to equation (1). Table 1 gives the solution coefficients for this formulation. All of the curves must merge to zero velocity at zero stress (for both P- and S-waves). Field results from Baker et al. (1999) and

Bachrach et al. (1998) are also plotted on Figure 1, attributed to some low-stress abscissa. The ovals an uncertainty about the actual stress conditions which would prevail over the travel path of the seismic waves. These data were recorded on the surface and are believed to be either horizontally propagating *P*-waves, head waves, or diving *P*-waves by their respective authors.

Because all the velocity curves merge at zero stress, there appears to be no lower bound on either *P*- or *S*-wave velocities. However, in my experience, natural soil deposits always have partial water saturation. If some water is present, cohesive forces will be present. Further, in real soil deposits there will be a diversity of grain sizes and often some clay or silt content (see the soil analysis, following). Soil cohesion from partial water or fines content provides an effective confinement and may be modeled as P_o in a modified version of equation (1):

$$V = C(P_o + P)^B. \qquad (2)$$

Figure 2 shows the result of fitting the Figure 1 data with equation (2). Solution coefficients are given in Table 2. The field data of White and Sengbush (1953) fit quite well, with *B* being quite close to the theoretical value of 1/6. The lab data for dry soil project to a near-sonic velocity. The near-saturated lab data are distinctly different from the other data, with a large P_o value in comparison with all other cases.

In summary, when capillary forces or other sources of cohesion are present, there may well be lower bounds for wave ve-

Table 1. Curve-fitting Figure 1: $V = C(P)^B$ (m/s), *P* in MPa.

Data set*	C	B
White *P*-wave	1176.8	0.179
White *SV*-wave	536.9	0.139
Khair *P*-wave, saturated	857.5	0.233
Khair *P*-wave, dry	664.3	0.209

*White = White and Sengbush (1953); Khair = Khair and Ibrahim (1999).
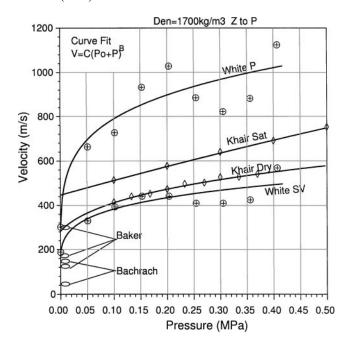

FIG. 2. Curve-fitting results with alternative power law that includes effective confinement to represent cohesion (see Table 2).

locities. In the case of Figure 2, these lower bounds for *P*-waves appear to be above the speed of sound in air. Future geophysical studies should include soil testing for water content, grain size, and Atterberg limits if the question of cohesion is to be addressed. (Atterberg limits are the water content values at key transition points in the mechanical behavior of cohesive soils. Two important limits mark the transitions from solid to plastic and plastic to liquid behavior.)

EXPERIMENTAL DESIGN

The experimental design employed geophones and instruments available for student field use. A bare spot in the university lawn was chosen to minimize complications from roots. The work was done in three phases:

1) vertical impact source to replicate published subsonic *P*-wave studies;
2) horizontal impact source done at only a few points to obtain some definitive control on shear properties; and
3) soil testing to document the type of soil investigated and help analyze the seismic results.

Table 3 summarizes the specifications of the experiments and testing.

Seismic acquisition

Figure 3 shows the experiment in plan and cross-sectional views, and it indicates the polarity conventions (negative voltage for a trough on variable area wiggle plots). Only two 3C geophones were available for the work. A stationary geophone was located at coordinate 1.5 m. The other geophone moved to occupy stations at 5-cm intervals along the profile from coordinates 2.05 to 2.95 m. Tap tests were done to confirm polarity. With the possible exception of the airwave, all other recorded signals are considered to represent the ground motion at the point where the geophone spike was bonded to the soil (not the spatial location of the geophone elements). Since the spike was 7.6 cm long, the recorded ground motion is for an average over the first 7.6 cm of soil depth.

Acquisition followed the pattern of first taking a five fold record with the vertical impact source at coordinate 2.0 m, followed by a second recording with the source at 3.0 m. The moving geophone occupied stations from 2.05 to 2.95 m, each time recording separately from each source position before moving to the next station. Horizontal source efforts were recorded for the geophone at 2.95 m. At the end of the experiment, a 2-cm depression was observed at each source position (compaction of the soil from repeated source efforts). The reference geophone recorded every source effort to determine the degree of repeatability of the source and monitor variations in amplitude and triggering.

Table 2. Curve-fitting Figure 2: $V = C(P + P_o)^B$ (m/s), *P* in MPa.

Data set*	C	P_o	B
White *P*-wave	1212.0	0.000566	0.187
White *SV*-wave	583.3	0.002237	0.184
Khair *P*-wave, saturated	767.5	0.464646	0.707
Khair *P*-wave, dry	674.8	0.026386	0.239

*White = White and Sengbush (1953); Khair = Khair and Ibrahim (1999).

Soil testing

The soil tests followed American Society for Testing and Materials (1996) standard protocols and is summarized in Table 4. The grain-size distribution is shown in Figure 4. Like most soils, this soil is composed of a wide range of grain sizes. This fact should be kept in mind since the Hertz-Mindlin theory is for a uniform (single) grain-size medium. Iwasaki and Tatsuoka (1977) observed a decrease in dynamic elastic modulus for an increase in uniformity coefficient. Thus, Hertz-Mindlin calculations might tend to underestimate velocities for real soils with diverse grain sizes.

Our soil was collected at the middle of the profile for sand cone testing (density and porosity). The hole was 6 inches in diameter with a depth of about 5 inches. After determining unit weight, the sample was split up for the remaining tests. The soil was found to be a sandy silt (unified classification ML). This is not a uniform soil but consists of a mix of grain sizes (38% sand, 57% silt, 5% clay). Given the significant partial water

Table 3. Data acquisition parameters and testing standards.

	Seismic
Vertical source	0.38-m, 0.75-kg steel dowel pressed to ground with about 5 N force. Dowel diameter is 0.01905 m (3/4 inch) with circular cross-section. Struck on free end with 0.2-kg ball peen hammer
Horizontal source	Same steel dowel and hammer. Blows struck horizontally at about 2 cm above ground level transverse to the line of profile.
Trigger	Contact closure of electrified hammer head and dowel.
Instruments	9048 Bison Engineering seismograph, recording 6 channels at 0.0001-s sample interval, 2500 samples per channel. Analog filters set at 4 Hz low cut and 2000 Hz high cut. Low cut is 2-pole Butterworth, High cut is 6-pole Butterworth. A 3.10-Hz high-pass RC follows field filters (hard-wired). Maximum dynamic range of about 90 dB.
Stationary geophone	3C Mark Products, 8 Hz, L10-A elements.
Moving geophone	3C OYO, 28 Hz, SMC-28-720, Sensitivity 24.43 V/(m/s) above 28 Hz.
	Soil Testing
Unit weight	Sand cone ASTM D-1556-90
Atterberg limits	ASTM D4318-95
Water content	ASTM D4643-87
Grain-size distribution	ASTM D-422-63
Specific gravity solids	ASTM D-854-83

Table 4. Soil testing results.

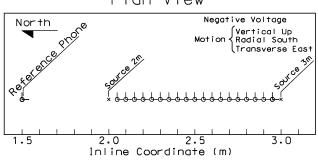| Property	Determined value
Liquid limit (LL)	46%
Plastic limit (PL)	36%
Plasticity index (PI)	10%
Grain density (kg/m^3)	2694
Water content	27.4%
Degree water saturation	63%
Void Ratio	1.168
Porosity	54%
Uniformity coef. (Cu)	16.7
Coef. of gradation (cc)	1.85
Unified classification	Sandy silt (ML)

FIG. 3. Experimental geometry in cross-section and plan view. Only two 3C geophones were used. The reference geophone remained stationary at coordinate 1.5 m. The moving geophone traveled between the two source positions. Common source position gathers yield reverse profiles.
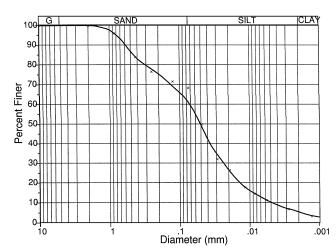

FIG. 4. The standard grain-size distribution. The soil is a sandy silt (ML, unified system).

saturation and presence of fines, one would expect cohesion to be present in this soil and that some lower bounds on wave velocity would exist as illustrated in Figure 2. Readers unfamiliar with soil testing and classification schemes are referred to Das (1993), a standard text on soil mechanics.

DISCUSSION

Vertical impact source

The vertical component data were sorted by source position (Figure 5). The top two records are common source position gathers for the moving geophone. Each trace has been scaled by the *L*2 norm (trace equalized) to overcome the limited dynamic range of a plot display. Signals recorded from the vertical component of the reference geophone are plotted below the common source gathers in true amplitude. One can observe the repeatability of the source in amplitude, waveform, and triggering stability. While not perfect, it is quite good for blows delivered freehand. The data have had no additional filtering, and the visible waveforms are for the largest-amplitude waves.

At first glance, these data look like what one might expect for a reverse-profile refraction experiment. It would be easy to pick first arrivals and perform a dipping refractor solution; the result of such an exercise is shown in Figure 6. However, this solution is defective. These waves are not refracted *P*-waves traveling at subsonic velocities. The pitfall lies in the wrong identification of the wave type.

It is important to consider two polarization characteristics of a refracted arrival. First, a compressive pulse which is either a direct or refracted wave should produce an initial upward ground motion and hence a negative voltage. However, a positive voltage indicates the first major motion is downward in Figure 5. Second, the first arrivals have the largest recorded amplitudes. For a downward vertical blow, approximately 93% of the energy is expected to be Rayleigh and *SV*-waves (Miller and Pursey, 1955). What little energy is radiated

as *P*-waves will have the smallest amplitude on the vertical geophone (Appendix). Lamb (1904) refers to *P*- and *SV*-waves as minor tremors and to the Rayleigh wave as the major tremor. Finally, if we consider the radiation pattern, we should expect a large fraction of the *P*-wave energy to be directed downward, below the source and away from our receivers (Appendix).

Spectral content, wavelengths, and dynamic range

First, the raw data were examined for digital clipping. None of the signals had been clipped during recording, and any apparent clipping in Figure 5 is plotter clipping. Since the dynamic range of the instrument is far greater than what is conveyed from a single wiggle plot, high-frequency *P*-waves might be hidden by the lower-frequency, large-amplitude data. Figure 7 shows a 30th-order maximum entropy spectrum for the source at coordinate 2 m and the receiver at 2.05 m (5 cm offset). Also shown in the inset is a 400th-order detailed estimate of the low frequencies. Note that the data peak at a frequency of 100 Hz. Thus, the refraction interpretation shown in Figure 6 has an additional defect, as this suggests. The wavelengths are too large
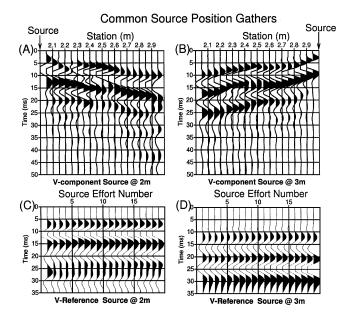

FIG. 5. (a, b) Trace-equalized vertical-component reverse profiles. (c, d) True-amplitude reference geophone traces demonstrate good repeatability of the source and the triggering.
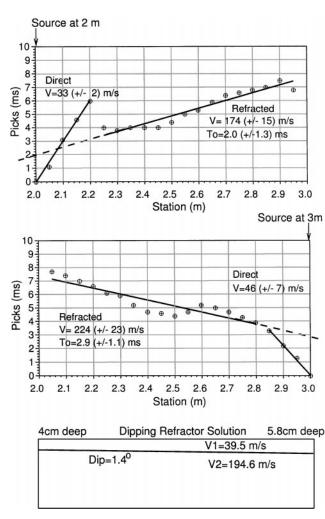

FIG. 6. Defective face-value solution of the dipping-bed refraction analysis of first-break picks. Top panel: forward profile first-arrival picks. Middle panel: reverse profile first-arrival picks. Bottom panel: defective face-value solution of the dipping-bed refraction analysis.

for a raypath interpretation. That is, wavelengths range from 0.4 to 2.0 m, but the first layer is only 0.04–0.06 m thick.

It is important to further examine the data in Figure 5 for higher-frequency P-waves. Filter panels were calculated using minimum-phase filters to prevent mixing later wave types with earlier arrivals, as would occur with zero-phase band-pass filters. To keep track of the phase delay introduced by band-pass minimum-phase filters, the data were augmented with three traces of delta functions, which were filtered to replicate the Bison analog filters (Table 3). Any delays introduced by the minimum-phase filters are then readily observable in the delays of the three filtered impulses.

Figure 8 shows filter panels for the vertical component data recorded by the moving geophone (source at 2 m). The bandwidth is 100 Hz in every case, and the center frequency is shown at the upper left of each panel. Based on wavelength, we expect that the data below 200 Hz may be in the near-field. Above 200 Hz but less than 1200 Hz, the panels exhibit coherent but often dispersive wavefields. With hodogram analysis, these waves can be shown to be high-frequency Rayleigh waves. Above 1000 Hz, we have a nondispersive coherent arrival which exhibits hyperbolic NMO. These arrivals are airwaves traveling from the free end of the dowel directly to the receiver stations. The discussion will begin with the airwave (first coherent arrivals) and then work down to lower frequencies.

Airwave analysis

The least-squares traveltime fit of the high-frequency vertical component arrivals is plotted in Figure 9a. The picks have been corrected for filter delays (analog and digital) and are for 1600- to 2400-Hz frequency. The solution assumed straight-line raypaths from the tip of the dowel to the geophone. The unknowns were the height of the source point above ground level and the velocity of wave propagation. Estimated uncertainties are for 95% confidence. The solution velocity, 321 ± 38 m/s, is in good agreement with the accepted value of 331 m/s for a P-wave in air. The solution for the height of the source point,

0.44 ± 0.2 m, agrees with the known height, 0.38 m. The filtered data are shown in Figure 9b.

Figure 10 shows a hodogram for the airwave arrival. The phone was at 0.3 m offset from the source. Consistent with a source point above the phone, we note the motion is mostly vertical. It is unclear how many of the signals represent ground motion and how many are acoustic pick-up at the phone elements.

Waves in the 200- to 1200-Hz band

The middle-frequency data in Figure 8 exhibit horizontal velocities that range from 40 to 250 m/s. Are these subsonic P-waves? We begin by observing the stretch in the waveforms, which suggests a degree of dispersion. Dispersion would be consistent with Rayleigh waves (assuming a pressure gradient produces an increase in velocity with depth).

The hodograms shown in Figure 11 correspond to the 400-Hz frequency panel of Figure 8. The geophone station was offset 0.5 m from the source. The major motion is elliptical retrograde in the vertical–radial plane, as would be expected for a Rayleigh wave and the basic solution to Lamb's problem (Appendix). Since the radiation pattern for the vertical impact favors Rayleigh and SV-waves over P-waves, it is not surprising that an earlier P-wave is not evident. If a diving P-wave with initial particle motion in the direction of the wave propagation
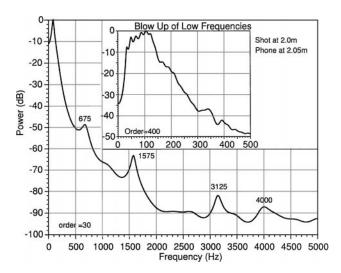

FIG. 7. Maximum entropy spectral estimates for the geophone 5 cm from the vertical impact source. The peak at 675 Hz corresponds to Rayleigh waves. A direct airwave with hyperbolic moveout corresponds to the peak at 1575 Hz (see filter panels). Inset: a detailed, high-order estimate of the low-frequency spectrum.
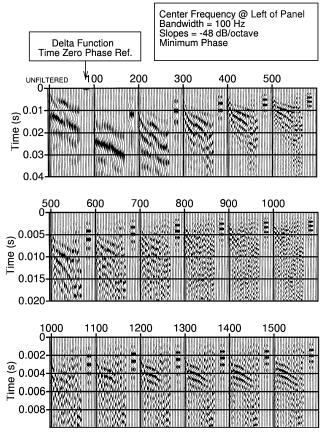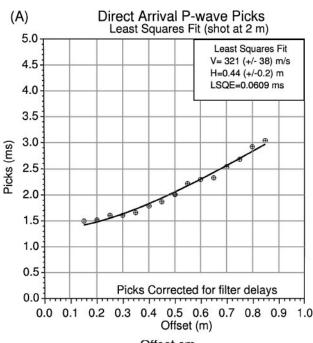

FIG. 8. Vertical-component data filter panels, source at 2.0 m. First panel is unfiltered. Center frequency is shown at upper left of each panel. Data are augmented with band-limited delta functions to observe the delay introduced by minimum-phase filters (see text). Note the changes in the vertical scale with increasing frequency.

were returning to the surface, a negative first motion would be seen on the vertical geophone (not positive, as is observed and expected for a horizontally propagating *SV*–Rayleigh-wave sequence).

Waves in the 100-Hz band

The hodograms in Figure 12 correspond to the 100-Hz panel of Figure 8. These motions represent the data in the earlier, face-value refraction interpretation. Here, the wavelengths are about 2 m, or twice the entire spread length, and under these conditions suggest observations in the near-field. The particle motions are large in all the views. This lack of recognizable polarization would be expected in the near-field, since all the wave motions which lead to far-field *P*- and *S*-waves overlap and are mixed at this offset. The significant transverse motion may be a combined result of a nonzero Poisson's ratio, less-than-perfect vertical orientation of the source dowel, tilt of the geophone, or off-line scatterers.
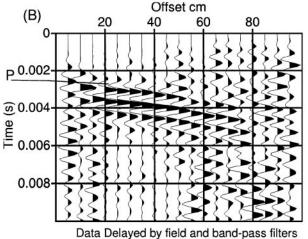

FIG. 9. (a) Traveltime solution for (b) high-frequency waves. Unknowns were hyperbolic moveout velocity and source height above ground. Solution supports airwave identification.

In Figure 12a, the motion begins as would be expected for a Rayleigh wave (retrograde, vertical elliptical motion). Then after about 25 ms, it shifts into the horizontal plane. The major axis, observed in Figure 12c, is not clearly aligned with either *P*- or *SH*-wave expectations but lies somewhere in between. Although these hodograms are complex and difficult to interpret,
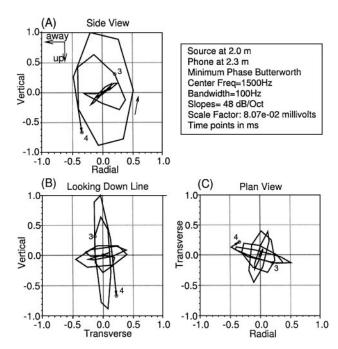

FIG. 10. Hodograms for high-frequency airwaves. Particle motion (a) in north-south vertical plane, (b) in east-west vertical plane, (c) in horizontal plane. Data are from 0.3 m offset of 1500-m/s panel of Figure 8.
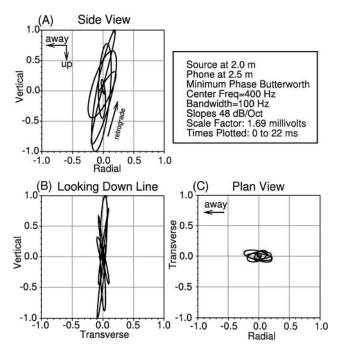

FIG. 11. Hodograms for 400-Hz band data of Figure 8. Particle motion (a) in north-south vertical plane, (b) in east-west vertical plane, (c) in horizontal plane. The major motion (a) is elliptical retrograde, as is expected for a Rayleigh wave. Offset = 0.5 m.

their complexity suggests that the data are in the near-field. The hodograms, however, are not consistent with the arrival of a direct *P*-wave, supporting the view that the earlier refraction interpretation was indeed defective.

SH-wave experiment

The source rod was struck near the ground horizontally from opposite directions to confirm *SH*-wave motion and velocities which could then be compared with any candidate subsonic *P*-waves. Figures 13a, c show recordings made with the geophone at station 2.95 m. The reference geophone recordings are shown in Figures 13b, d. Two traces are displayed in each plot; these are transverse geophone signals from both source polarizations. Where the traces depart in opposite directions indicates the first arrival of the *SH*-wave. On this basis, arrival times were picked and are shown in each plot. The horizontal velocities were computed from the source at 2 and 3 m. The resulting *SH*-wave velocities were 164 and 138 m/s, respectively. The average of these two velocities is 150 m/s, somewhat slower than the observed velocities on the vertical component data for the incorrectly identified *P*-refraction (194.6 m/s). Such a difference between vertical and horizontal shear velocities is to be expected. The different horizontal and vertical stresses will produce shear-wave speeds that are dependent on the wave polarization (Richart et al., 1970; Roesler, 1979; Yu and Richart, 1984). Further, *SH*-waves can be trapped in shallow wave guides and exhibit slower speeds than Rayleigh and *SV*-waves.

This suggests another potential pitfall for wave identification when only one or two components of motion are available. Since *SH*-waves are often slower than Rayleigh waves, it is possible to mistake the faster Rayleigh waves as *P*-waves when only vertical and transverse motions are viewed. Thus, it is important to examine the radial motion to avoid this trap.

Dynamic levels of strain affect velocity

While ambient effective stress is an important factor in determining wave velocity, the magnitude of the dynamic strain produced by the source is also relevant. The dependence of *S*-wave velocities on strain magnitude is well documented in the literature, both in the laboratory and in the field (Seed et al., 1986; Salgado et al., 1997). The expectation is that near the source, the velocity is slower because of the larger dynamic strains. Once the dynamic levels of strain have fallen below about 0.001%, conditions of small strain have been met.

One may compute the dynamic strain levels from the signal amplitudes in seismic traces. The strain is calculated from the unitless ratio,

$$\varepsilon = \frac{v}{V} \tag{3}$$

where ε is the dynamic strain, v is the particle velocity, and V is the phase velocity of the wave (White, 1965, p. 22). Wave velocity c is computed from the dip in time (requires several traces). To compute v, one multiplies the sensitivity of the geophone with the voltages recorded. For the vertical component data in Figure 5 at offsets >0.3 m, the strain levels have nominally fallen off to the 0.001% range. This indicates that the far-offset velocities are largely strain independent. Within 0.3 m of the source, the larger strain levels result in reduced shear velocity. These slower near-source velocities may have contributed to the illusion of a direct subsonic *P*-wave in the Figure 5 data.
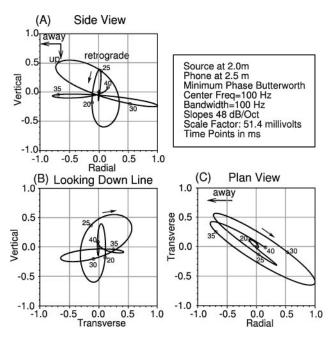

FIG. 12. Hodograms for 100-Hz band data of Figure 8. Particle motion (a) in north-south vertical plane, (b) in east-west vertical plane, (c) in horizontal plane. The initial motion appears elliptical retrograde (a) but quickly becomes more complicated. Amplitudes are large in all directions, typical of the near-field. Offset = 0.5 m.
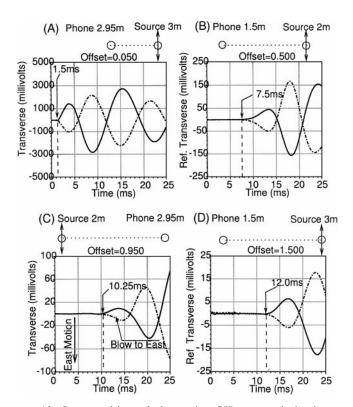

FIG. 13. Superposition of alternative *SH*-wave polarizations as recorded on transverse geophones. *SH*-wave arrivals are picked at the point where the traces depart. Different offsets are shown: (a) 0.05 m, (b) 0.5 m, (c) 0.95 m, (d) 1.5 m.

CONCLUSIONS

The existence of subsonic *P*-waves was not confirmed in this study. Both theoretical and hodogram analyses suggest that near-field, Rayleigh, and *SV*-waves might easily be mistaken for subsonic *P*-waves. This experiment indicates the presence of near-field and Rayleigh waves on the vertical component with velocities ranging from 40 to 200 m/s. To properly identify a first arrival, one needs multicomponent data to confirm the actual particle motion. Using polarizable sources also helps confirm *S*-wave velocities, which then can be used for comparison with any candidate subsonic *P*-wave.

One might ask, Where are the *P*-waves if they are not the first arrivals? The answer involves radiation patterns and an understanding of the near-field. The wave disturbance must propagate some distance before *P*-waves emerge. Aki and Richards (1980) make this point: "… it is not always fruitful to decompose an elastic displacement field into its *P*-wave and *S*-wave components" (p. 76). Here, no *P*-waves were observed propagating in the soil within 1 m of the source. While one might expect that the *S*-wave velocities observed in this study would predict subsonic *P*-wave velocities for a reasonable Poisson's ratio, these *P*-waves would be overwhelmed by the Rayleigh-wave motions (Appendix).

The combined effect of a low Poisson's ratio (which would result in less vertical motion for a horizontally propagating *P*-wave), the very low level of *P*-radiation (only 7%, most of which is directed away from the receivers), and the lack of geophone arrays may combine to place *P*-waves outside the dynamic range of the recorder (the gain of which is set to avoid clipping the largest amplitude signals). While future investigations might invoke the use of geophone arrays, some degradation of direct arriving *P*-waves would be inevitable. A better approach might be to use subsurface (downhole) methods to escape the interference of large-amplitude boundary waves on the surface.

Actually, the lack of *P*-waves is an advantage to those practicing engineering geophysics. Shear and surface waves may be more useful than *P*-waves. They relate well not only to the soil frame but also to the interaction between pore fluids and the frame via the complex modulus (Stoll, 1985; Michaels, 1998).

ACKNOWLEDGMENTS

Thanks to the students in applied geophysics who helped collect the data for this study and to Boise State University for not turning on the sprinklers during the experiment. An anonymous reviewer provided many helpful comments. Further thanks go to the authors of Seismic Unix (Colorado School of Mines), Scilab (France), and the Linux operating system (too many to list), which were used in the processing of the data. Khair and Ibrahim data are reprinted with permission from the Journal of Environmental and Engineering Geophysics (March 1999), a publication of the Environmental and Engineering Geophysical Society. Center for Geophysical Investigation of Shallow Subsurface contribution 0103.

REFERENCES

Aki, K., and Richards, P. G., 1980, Quantitative seismology, vol. 1: W. H. Freeman & Co.
American Society for Testing and Materials, 1996, Annual book of ASTM standards, section 4—Construction, vol. 4.08, Soil and rock (I): Am. Soc. Test. Mat., D420–D4914.
Bachrach, R., and Nur, A., 1998, High-resolution shallow seismic experiments in sand, part I—Water table, fluid flow, and saturation: Geophysics, **63**, 1225–1233.
Bachrach, R., Dvorkin, J., and Nur, A., 1998, High-resolution shallow seismic experiments in sand, part II—Velocities in shallow unconsolidated sands: Geophysics, **63**, 1234–1240.
——— 2000, Seismic velocities and Poisson's ratio of shallow unconsolidated sands: Geophysics, **65**, 559–564.
Baker, G. S., Steeples, D. W., and Schmeissner, C., 1999, Case history—In-situ, high-frequency *P*-wave velocity measurements within 1 m of the earth's surface: Geophysics, **64**, 323–325.
Cascante, G., and Santamarina, C. J., 1996, Interparticle contact behavior and wave propagation: J. Geotech. Eng., **122**, No. 10, 831–839.
Das, B. M., 1993, Principles of geotechnical engineering, 3rd ed.: PWS Publ. Co.
Gassmann, F., 1951a, Über die Elastizität poroser Medien: Vierteljahrsschrift der Natürforschenden Gesellschaft in Zurich, **96**, 9–23.
——— 1951b, Elastic waves through a packing of spheres: Geophysics, **16**, 673–685.
——— 1953, Errata to Geophysics, vol. 16, no. 4. paper: Geophysics, **18**, 269.
Hertz, H., 1881, Über die beruhrung fester elastischer Korper: J. für die Reine und Angewandte Mathematik, **92**, 156–171.
Iwasaki, T., and Tatsuoka, F., 1977, Effects of grain size and grading on dynamic shear moduli of sands: Japan. Soc. Soil Mech. and Found. Eng., **17**, No. 3, 19–35.
Khair, K., and Ibrahim, A., 1999, The velocity of elastic *P*-waves in unconsolidated material under low pressure: J. Env. Eng. Geophys., **4**, 1–9.
Lamb, H., 1904, On the propagation of tremors over the surface of an elastic solid: Phil. Trans. Roy. Soc., **A203**, 1–42.
Michaels, P., 1998, In situ determination of soil stiffness and damping: J. Geotech. Geoenv. Eng., **124**, 709–719.
Miller, G. F., and Pursey, H., 1954, The field and radiation impedance of mechanical radiators on the free surface of a semi-infinite isotropic solid: Proc. Roy. Soc., **A223**, 521–541.
——— 1955, On the partition of energy between elastic waves in a semi-infinite solid: Proc. Roy. Soc., **A233**, 55–69.
Mindlin, R. D., 1949, Compliance of elastic bodies in contact: J. Appl. Mech., **16**, 259–268.
——— 1954, Mechanics of granular media: Columbia University Tech. Report 14, ONR Project NR-064-388.
Mindlin, R. D., and Deresiewicz, H., 1953, Elastic spheres in contact under varying oblique forces: J. Appl. Mech., 327–344.
Mooney, H. M., 1974, Some numerical solutions for Lamb's problem: Bull. Seis. Soc. Am., **64**, No. 2, 473–491.
Pekeris, C. L., 1955, The seismic surface pulse: Proc. Nat. Acad. Sci., **41**, 469–480.
Richards, P. G., 1979, Elementary solutions to Lamb's problem for a point source and their relevance to three-dimensional studies of spontaneous crack propagation: Bull. Seis. Soc. Am., **69**, No. 4, 947–956.
Richart, F. E., Jr., Hall, J. R., Jr., and Woods, R. D., 1970, Vibrations of soils and foundations: Prentice-Hall, Inc.
Roesler, S. K., 1979, Anisotropic shear modulus due to stress anisotropy: J. Geotech. Eng., **105**, 871–881.
Salgado, R., Drnevich, V. P., Ashmawy, A., Grant, W. P., and Vallenas, P., 1997, Interpretation of large-strain seismic cross-hole tests: J. Geotech. Geoenv. Eng., **123**, No. 4, 382–388.
Sanchez-Salinero, I., Roesset, J. M., and Stokoe, K. H., 1986, Near-field effects on determination of propagation velocities of body waves: 56th Ann. Internat. Mtg., Soc. Expl. Geophys., Expanded Abstracts, 129–131.
Seed, H. B., Wong, R. T., Idriss, I. M., and Tokimatsu, K., 1986, Moduli and damping factors for dynamic analysis of cohesionless soils: J. Geotech. Eng., **112**, 1016–1032.
Stoll, R. D., 1985, Computer-aided studies of complex soil moduli, *in* Woods, R. D., Ed., Measurement and use of shear wave velocity for evaluating dynamic soil properties: Am. Soc. Civil Eng., 18–33.
White, J. E., 1965, Seismic waves, radiation, transmission and attenuation: McGraw-Hill, Book Co.
——— 1983, Underground sound, application of seismic waves: Elsevier Science Publ. Co., Inc.
White, J. E., and Sengbush, R. L., 1953, Velocity measurements in near-surface formations: Geophysics, **18**, 54–69.
Wu, S., Gray, D. H., and Richart, F. E., Jr., 1984, Capillary effects on dynamic moduli of sands and silts: J. Geotech. Eng., **110**, 1188–1203.
Yu, P., and Richart, F. E., Jr., 1984, Stress ratio effects on shear modulus of dry sands: J. Geotech. Eng., **110**, 331–345.

APPENDIX A
LAMB'S PROBLEM

The use of hodograms to identify waves requires a basic understanding of the expected motions for different wave types. Lamb's original work (1904) addressed the waves propagating on the surface of an elastic, homogeneous half-space from a vertical impact point source. That work has inspired a number of studies into both the resultant body wave radiation and the inhomogeneous waves traveling on the surface.

Figure A-1a illustrates the approximate body-wave radiation patterns produced for the far-field from a circular radiator of small diameter (Miller and Pursey, 1954, equations 116 and 117). P-waves are radiated downward, and SV-waves are radiated off to the sides. The specific case is for a Poisson's ratio of 1/4 ($V_p/V_s = 3^{1/2}$). There are two SV-wave lobes to each side of the radiation pattern. The boundary between lobes is at about 35° from the vertical. The waves in the lobe labeled SV-I are phase shifted by 90° relative to the lobe labeled SV. Figure A-1b shows the typical horizontal and vertical motion for the Rayleigh waves radiated on the surface. In addition to the major-tremor Rayleigh waves, Lamb also predicted both P- and SV-waves would radiate along the surface as minor tremors.

A number of authors have examined Lamb's solution (Pekeris, 1955; Mooney, 1974; Richards, 1979). This solution is most relevant to geophones near the source on the ground surface. Figure A-2 shows the relevant vertical and horizontal motions as a function of normalized unitless time τ,

$$\tau = \frac{V_s t}{R}, \qquad (A-1)$$

where R is the horizontal distance from the source, V_s is the S-wave velocity, and t is time in seconds. This solution was computed by recreating the computer program described by Mooney (1974) for an elastic half-space with a Poisson's ratio of 1/4, the source being a step function. Figure A-2 matches 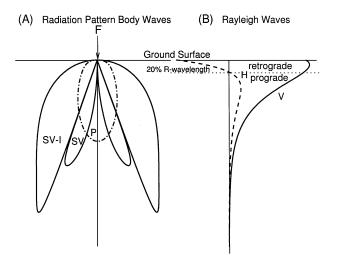the results shown in Mooney (1974, Figure 2), Pekeris (1955, Figures 3 and 4), and Richards (1979, Figures 2 and 3, integrals I_3 and I_4, respectively). The Rayleigh-wave response has been clipped to match Mooney's figure (for ease of comparison) and to reveal the vastly lower-amplitude P- and SV-waves.

Synthetic seismograms are computed by differentiating the step function response (gives impulse response), convolving with a wavelet, and then differentiating to simulate the output of a velocity geophone. Figure A-3 shows such a calculation for an S-wave velocity of 150 m/s and a receiver at 150 m offset (this makes it easier to relate Figures A-2 and A-3 since unitless time and time in seconds have the same numerical value).
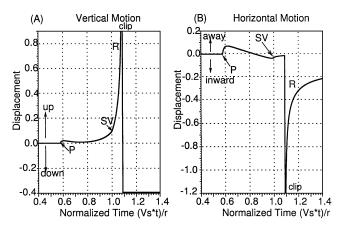

FIG. A-2. Solution to Lamb's problem (after Mooney, 1974), showing (a) vertical and (b) horizontal displacement as a function of normalized (unitless) time. Source is a step function. Rayleigh wave has been clipped to permit viewing the much lower-amplitude P- and SV-wave motions.
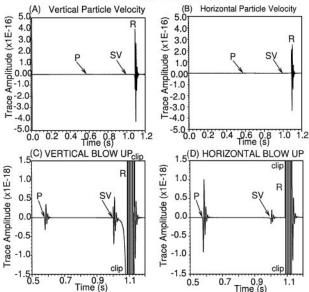

FIG. A-3. Far-field geophone response (particle velocity). P- and SV-waves are too small to be seen in (a) and (b) but can be seen if the Rayleigh wave is clipped (c, d).

FIG. A-1. (a) Approximate directivity patterns for far-field P- and SV-waves in an elastic half-space, vertical point-source function. (b) Typical vertical and horizontal displacement eigenfunctions for a Rayleigh wave (after Miller and Pursey, 1954).

The wavelet had a center frequency of 100 Hz, and the polarity convention gives a negative voltage upward or away from the source motion. The vertical and horizontal signals illustrate the degree to which the Rayleigh wave dominates in amplitude (the *P*- and *SV*-waves are too small to be seen, but their positions are indicated with arrows). Figures A-3c, d reveal the *P*- and *SV*-waves but require clipping the Rayleigh wave plot. In the absence of geophone arrays, it appears likely that direct *P*- or *SV*-wave amplitudes may be below the recording threshold if the gain is set to avoid clipping the Rayleigh wave.

Figure A-4 shows hodograms plotted from the Figure A-3 signals, as well as the wavelet used in the calculations. The *P*-wave motion (Figure A-4a) is very narrow prograde elliptical, with the vertical motion being less than the radial (and this depends on Poisson's ratio). The *SV*-wave motion (Figure A-4b) is a more open ellipse than for the *P*-wave, with the major motion in the vertical direction. The Rayleigh-wave motion (Figure A-4c) is like the *SV*-motion but even more open than the *SV*-wave and significantly larger in amplitude.

Near-field and Lamb's problem

Figures A-3 and A-4 were calculated for the far-field (about 100 *S*-wavelengths), where Rayleigh, *P*-, and *SV*-waves have separated for the given duration of the seismic wavelet, 50 ms. When one considers the region near the source, the various arrivals may overlap in time. The synthetic seismogram (Figure A-5a) with a 0.5-m trace spacing was computed for Lamb's problem and illustrates the transition from near- to far-field. The *SV*-velocity is 150 m/s, with the 100-Hz wavelet of Figure A-4 (wavelength 1.5 m). The *P*-wave (259.8 m/s) becomes distinct at about 2 m and becomes completely separate
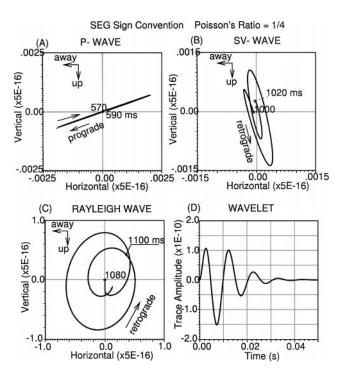
from the *SV*- and Rayleigh-wave arrivals at 10 m offset from the source. The near-field offsets are expanded in Figure A-5b with a synthetic recomputed at a 5-cm trace spacing. The first motion changes from positive (black) to negative at about 25 cm. As the computed *P*-wave arrival separates from the *SV*-wave and the larger Rayleigh wave, the first motion negative increases in amplitude and the waveform stretches, producing near-field dispersion. This particular case assumes that subsonic *P*-waves are possible for an *SV*-wave velocity of 150 m/s and a Poisson's ratio of 1/4.

Data from the experiment discussed in this paper are shown in Figure A-5c. The first motion appears to be positive for the

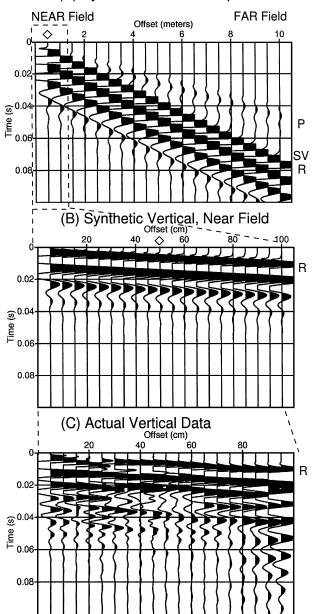FIG. A-4. Particle velocity hodograms for Figure A-3 synthetic seismograms. (d) Wavelet.

FIG. A-5. Multioffset synthetics from the solution to Lamb's problem. (a) Near- and far-field motions. (b) Near-field synthetic vertical data. (c) Recorded field data of the study.

entire first meter, suggesting that any possible subsonic P-wave has not been recorded. Of course, Poisson's ratio might be less than 1/4, and a subsonic P-wave could still be hidden in the major Rayleigh-wave motion. If Poisson's ratio were zero, then the slowest possible P-wave would be 212 m/s. This would mean that the P-wave would arrive only 2 ms before the Rayleigh wave at a 1-m offset. At the other extreme would be a Poisson's ratio of about 0.49, predicting a P-wave velocity of >1070 m/s, which we should see emerging ahead of the Rayleigh wave.

We conclude that we are in the near-field and have not observed subsonic P-waves, perhaps because they are hidden by the much larger Rayleigh wave or because they cannot exist in that zone of the radiation pattern. An improved experiment that might be capable of subsonic P-wave detection should include a wider range of offsets (to permit far-field observations) and placement of the receivers in a more favorable zone of the radiation pattern (below or above the source position, in the subsurface).